# Development of Meshfree Method for Slope Stability and Post-Failure Analyses

On-Lei Annie Kwok[1], *Pai-Chen Guan[2], Wei-Po Cheng[3] Chun-Ting Sun[4]

[1], [3] *Department of Civil Engineering, National Taiwan University, Taipei 10617, Taiwan*
[2], [4] *Department of Systems Engineering and Naval Architecture, National Taiwan Ocean University, Keelung 20224, Taiwan*
[1] *annieonleikwok@ntu.edu.tw*, [2] *paichen@ntou.edu.tw*

## ABSTRACT

Limit equilibrium methods (LEM) are often used in practice to evaluate slope stability in terms of factor-of-safety. With advances in computational methods and rapid developments in computer software and hardware, finite element (FEM) or finite difference methods (FDM) are increasingly utilized to analyze slope stability (Griffiths and Lane, 1999). The advantages of FEM and FDM over LEM are that there is no need to make any assumption about the critical slip surface (e.g. location and shape), and quantities such as stress, strain, displacements, pore pressures in slopes, can be calculated.

In recent years, a numerical scheme called the meshfree method has been developed. The main difference between meshfree method and conventional FEM/FDM is that no mesh is necessary throughout the analysis process. While retaining the benefits of conventional numerical schemes, meshfree method can be more advantageous when problems with large deformation are encountered. This is because accuracy of solution is often lost when there is significant mesh distortion. In this paper, a meshfree method named Semi-Lagrangian Reproducing Kernel Particle Method (SLRKPM, Guan, et al., 2011) is developed to analyze several slope stability problems. Analysis results are compared to those from finite element methods. In addition, the potential for utilizing the meshfree method in geotechnical problems with large-deformation, e.g., the post-failure behavior of slope, is explored and discussed.

## INTRODUCTION

In the last few decades, computational methods such as finite element method (FEM) and finite difference methods (FDM) has become more popular in geotechnical engineering practice due to advances in computer hardware and development of commercial software. Numerical modeling is especially useful when no simplified

---

[1],[3] Assistant Professor
[2],[4] Graduate Student

theoretical solution is available, for example, slope stability with complex geometry and heterogeneous soil layers, staged excavation of soil with dewatering etc.. However, most numerical formulations can only model up to the point of failure or allow finite deformation. In recent years, meshfree method (e.g Liu et al., 1995; Chen et al., 1996) has been developed extensively. As suggested by its name, no mesh is required when the numerical modeling is performed. This would be attractive when large deformation is encountered as numerical solution would not be affected by the problem of mesh distortion. In this paper, a recently developed meshfree formulation called "semi-Lagrangian reproducing kernel particle method" will be first discussed. Examples of slope stability problems analyzed by this new method will be presented. Finally, the capability of this method in analyzing geotechnical problem with large deformation will be demonstrated.

## THEORETICAL FORMULATION OF SEMI-LAGRANGIAN REPRODUCING KERNEL PARTICLE METHOD

### Governing Equations

The semi-Lagrangian Reproducing Kernel Particle method (SLRKPM, Guan, et al., 2011) is a modified approach based on the Total Lagrangian or Updated Lagrangian governing equations. To employ path dependent material behavior, here we derive the weak form by using the Updated Lagrangian form. Consider a continue body occupying domain $\Omega_X$, with Dirichlet boundary $\Gamma_X^g$ and Neumann boundary $\Gamma_X^h$. The deformed body occupies $\Omega_x$ with boundary $\Gamma_x^g$ and $\Gamma_x^h$. A mapping function $x = \omega(X,t)$ is defined to describe the motion of the body from the undeformed location $X$ to deformed location $x$. The weak form based on the principle of virtual power is as follows

$$\int_{\Omega_x} \delta v_i \rho \dot{v}_i d\Omega + \int_{\Omega_x} \frac{\partial(\delta v_i)}{\partial x_j} \sigma_{ij} d\Omega - \int_{\Gamma_x} \delta v_i \rho b_i d\Omega - \int_{\Gamma_x^h} \delta v_i h_i d\Gamma = 0 \qquad (1)$$

Where $\rho$, $v_i$, $\dot{v}_i$, $\sigma_{ij}$, $b_i$, $h_i$ are density, velocity, acceleration, Cauchy stress, body force and surface traction based on the deformed configuration. The lower case index $i$ represent the current coordinate $x$. The deformation gradient is defined as

$$F_{iJ} = \partial x_i / \partial X_J \qquad (2)$$

The gradient of each term in eqn. (1) with respect to current coordinate could be converted to the initial configuration as follows:

$$\int_{\Omega_x} \delta v_i \rho \dot{v}_i d\Omega = \int_{\Omega_X} \delta v_i \rho^0 \dot{v}_i d\Omega \qquad (3)$$

$$\int_{\Omega_x} \frac{\partial(\delta v_i)}{\partial x_j} \sigma_{ij} d\Omega = \int_{\Omega_X} \frac{\partial \delta v_i}{\partial X_K} F_{jK}^{-1} \sigma_{ij} J d\Omega = \int_{\Omega_X} \frac{\partial \delta v_i}{\partial X_K} P_{Ki} d\Omega \qquad (4)$$

$$\int_{\Omega_x} \delta v_i b_i d\Omega = \int_{\Omega_X} \delta v_i b_i J d\Omega = \int_{\Omega_X} \delta v_i b_i^0 d\Omega \qquad (5)$$

$$\int_{\Gamma_x^h} \delta v_i h_i d\Gamma = \int_{\Gamma_X^h} \delta v_i \sigma_{ij} F_{jK}^{-1} n_K^0 J d\Gamma = \int_{\Gamma_X^h} \delta v_i h_i^0 d\Gamma \qquad (6)$$

$\rho^0$ 、 $b_i^0$ 、 $h_i^0$ are initial density, body force, and surface traction, $J$ is the determinant of deformation gradient $F_{iJ}$, $n_K^0$ is the surface normal, $P_{ij}$ is the nominal stress

$$P = JF^{-1}\sigma \qquad (7)$$

*Reproducing Kernel Approximation*

Consider the deformed body occupying close domain $\bar{\Omega}_x = \Omega_x \bigcup \Gamma_x$ is discretized by a set of RK nodes *NP*. The function $u(\boldsymbol{x})$ within the domain $\bar{\Omega}_x$ can be approximated by the reproducing kernel approximation.

$$u^h(\boldsymbol{x}) = \sum_{I=1}^{NP} \Psi_I(\boldsymbol{x}; \boldsymbol{x} - \boldsymbol{x}_I) d_I \qquad (8)$$

where $u^h(x)$ is the approximation of the original function $u(x)$, $\Psi_I(\boldsymbol{x}; \boldsymbol{x} - \boldsymbol{x}_I)$ and $d_I$ are the RK shape function and nodal coefficient for node *I*. The RK shape function is constructed by the multiplication of a smoothed function called kernel function $\phi_a(\boldsymbol{x} - \boldsymbol{x}_I)$, and a polynomial based correction function.

$$\Psi_I(\boldsymbol{x}; \boldsymbol{x} - \boldsymbol{x}_I) = C(\boldsymbol{x}; \boldsymbol{x} - \boldsymbol{x}_I)\phi_a(\boldsymbol{x} - \boldsymbol{x}_I) \qquad (9)$$

The kernel functions determine the smoothness and the locality of the approximation. The kernel function is defined based on the distance from each RK node. The function is non-zero within an area called support region "*a*" and is zero elsewhere. An example of kernel function is as follows

$$z = \frac{\|\boldsymbol{x} - \boldsymbol{x}_I\|}{a}, \qquad \phi_a(z) = \begin{cases} 2/3 - 4z^2 + 4z^3 & \text{for } 0 \leq z \leq 0.5 \\ 4/3 - 4z + 4z^2 - \dfrac{4}{3}z^3 & \text{for } 0.5 \leq z \leq 1, \\ 0 & \text{for } z > 1 \end{cases} \qquad (10)$$

The correction function is the collection of polynomials up to the order *N*.

$$C(\boldsymbol{x}; \boldsymbol{x} - \boldsymbol{x}_I) = \sum_{i=0}^{N} b_i(\boldsymbol{x})(\boldsymbol{x} - \boldsymbol{x}_I)^i = \boldsymbol{H}^T(\boldsymbol{x} - \boldsymbol{x}_I)\boldsymbol{b}(\boldsymbol{x})$$

$$\boldsymbol{H}^T(\boldsymbol{x} - \boldsymbol{x}_I) = \left[1, (\boldsymbol{x} - \boldsymbol{x}_I)^1, (\boldsymbol{x} - \boldsymbol{x}_I)^2, ..., (\boldsymbol{x} - \boldsymbol{x}_I)^N\right] \qquad (11)$$

$$\boldsymbol{b}^T(\boldsymbol{x}) = \left[b_0(\boldsymbol{x}), \boldsymbol{b}^1(\boldsymbol{x}), \boldsymbol{b}^2(\boldsymbol{x}), ..., \boldsymbol{b}^N(\boldsymbol{x})\right]$$

where $(\boldsymbol{x} - \boldsymbol{x}_I)^i$ vector contains the complete *i*-th row of Pascal's triangle, and $\boldsymbol{b}^i(x)$ is the vector of associated unknown coefficients of $(\boldsymbol{x} - \boldsymbol{x}_I)^i$. To solve the coefficient vector $\boldsymbol{b}^T(x)$, the following consistency condition is imposed

$$\sum_{I=1}^{NP} \Psi_I(x) x_{1I}^i = x_1^i \quad , \qquad i \leq N \qquad (12)$$

The coefficient vector is obtained by solving the eqn.(12)

$$M(x)b(x) = H(0)$$

$$H(0) = [1, 0, ..., 0] \tag{13}$$

$$M(x) = \sum_{J=1}^{NP} H(x - x_J) H^T(x - x_J) \phi_a(x - x_J)$$

$$b(x) = M^{-1}(x) H(0) \tag{14}$$

Notice that constructing the moment matrix $M(x)$ requires to collect the neighbor points whose supports are covering the location $x$, as shown in Fig. 2. Substituting eqns. (14) and (11) into (9),

$$\Psi_I(x; x - x_I) = H^T(0) M^{-1}(x) H(x - x_I) \phi_a(x - x_I) \tag{15}$$
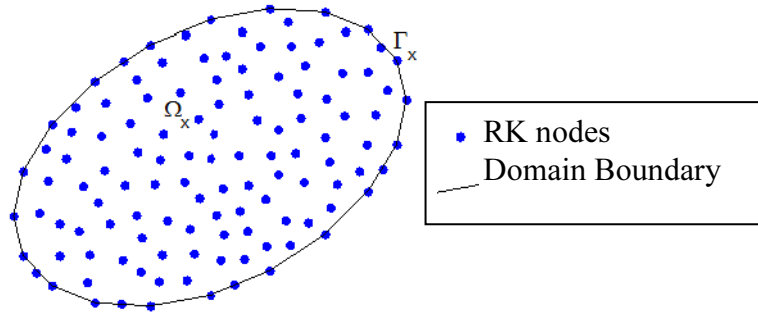


Fig. 1 RK discretization of domain $\Omega_x$
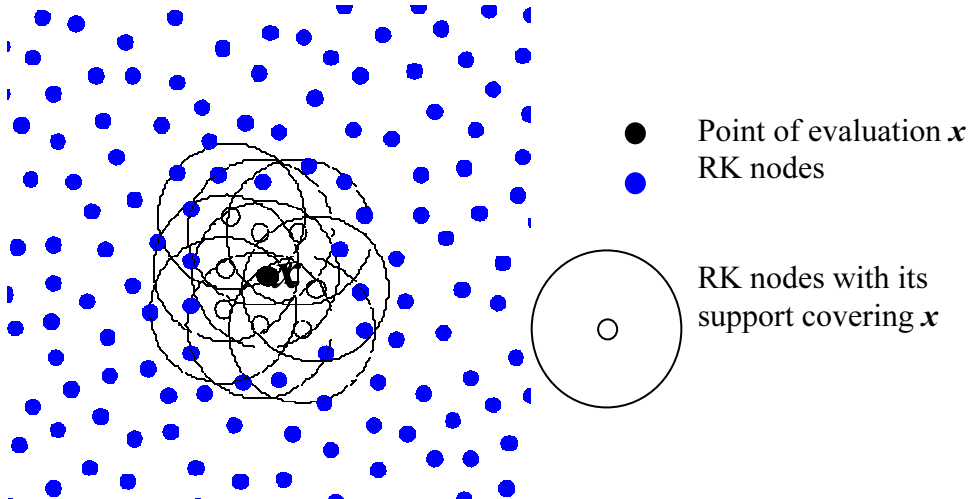


Fig. 2 Example of RK support and neighboring nodes for constructing moment matrix $M(x)$ in eqn (13)

*Semi-Lagrangian Reproducing Kernel Approximation*

The Lagrangian reproducing kernel particle method introduces the shape function based on the initial configuration

$$\Psi_I(X; X - X_I) = H^T(0) M^{-1}(X) H(X - X_I) \phi_a(X - X_I) \tag{16}$$

where $X_I$ are the original (un-deformed) location of the RK points. The deformed nodal location is approximated by the RK approximation

$$x = \omega(X,t) = \sum_{I=1}^{NP} \Psi_I(X; X - X_I) X_I \tag{17}$$

Substituting eqn. (17) into (2) we obtain

$$F_{ij} = \partial x_i / \partial X_j = \sum_{I=1}^{NP} \left( \frac{\partial \Psi_I(X)}{\partial X_j} \right) X_{Ii} \tag{18}$$

The mapping process by (17) is more stable comparing with standard FEM method. However, when extremely deformation occurs, such as land slide, debris flow and soil boiling process during liquefaction, the mapping by (18) breaks down if deformation loses positive definite property.

To avoid using the deformation gradient, the semi-Lagrangian reproducing kernel particle method (SLRKPM) is introduced.

Under the SLRKPM method framework, the RK shape functions are constructed under the deformed configuration.

$$\Psi_I(x; x - x_I) = H^T(0) M^{-1}(x) H(x - x_I) \phi_a(x - x_I) \tag{19}$$

where $x_I$ are the deformed location of the RK points. A comparison of Lagrangian kernels and semi-Lagrangian kernels is shown in Fig. 3. The reconstruction of kernel $\phi_a(x - x_I)$ under current configuration gives the flexibility of allowing neighbor nodes to be added in the moment matrix in eqn. (13). The semi-Lagrangian RK shape function is introduced to approximate the velocity

$$v_i^h = \sum_{I=1}^{NP} \Psi_I(x; x - x_I) v_{Ii} \tag{20}$$

Substituting eqn. (20) into eqns. (1), the governing equation is obtained after some derivation

$$M\dot{v} + Nv = f^{ext} - f^{int} \tag{21}$$

where

$$M_{IJ} = \int_{\Omega_x} \rho \Psi_I(x) \Psi_J(x) I d\Omega$$

$$N_{IJ} = \int_{\Omega_x} \rho \Psi_I(x) \Psi_J^*(x) I d\Omega$$

$$f_I^{int} = \int_{\Omega_x} B_I^T \sigma d\Omega \tag{22}$$

$$f_I^{ext} = \int_{\Omega_x} \Psi_I(x) b d\Omega + \int_{\Gamma_x^h} \Psi_I(x) h d\Gamma$$

and $I$ is the identity matrix, $B_I$ is the gradient matrix associated with $v_{(i,j)} = (v_{i,j} + v_{j,i})/2$, $\sigma$ is the stress vector associated with $\sigma_{ij}$, and $b$ and $h$ are body force and surface traction vectors, respectively. The time derivative of kernel leads to the following special term:

$$\Psi_I^*(\boldsymbol{x}) = C(\boldsymbol{x}; \boldsymbol{x} - \boldsymbol{x}_I) \dot{\phi}_a(\boldsymbol{x} - \boldsymbol{x}_I) \qquad (23)$$

$$\dot{\phi}_a(\boldsymbol{x} - \boldsymbol{x}_I) = \dot{\phi}_a\left(\frac{\|\boldsymbol{x} - \boldsymbol{x}_I\|}{a}\right) = \phi_a'\left(\frac{\|\boldsymbol{x} - \boldsymbol{x}_I\|}{a}\right)\frac{\boldsymbol{n} \cdot (\boldsymbol{v} - \boldsymbol{v}_I)}{a} \qquad (24)$$

where $\boldsymbol{v}_I$ is the nodal velocity vector and $\boldsymbol{n} = (\boldsymbol{x} - \boldsymbol{x}_I)/\|\boldsymbol{x} - \boldsymbol{x}_I\|$. The matrix $N_{IJ}$ is associated with the convective effect due to the relative motion of RK nodes. The significance of the convective term is discussed in Guan et. al. (2009). The temporal stability is affected by velocity gradient between RK nodes shown in eqn. (24). Higher velocity gradient leads to more restricted stability condition (smaller time step).
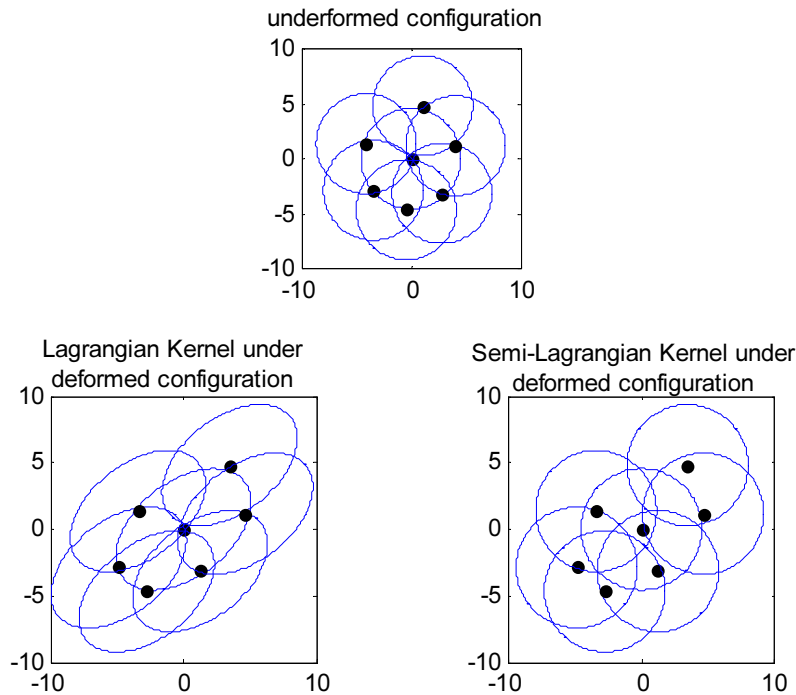


Fig. 3 Comparison of Lagrangian and Semi-Lagrangian kernel under deformation.
Black solid circle: RK nodes; Blue circle: RK support

## SLOPE STABILITY ANALYSES

The semi-Lagrangian reproducing kernel particle formulation presented in previous section is coded in a Fortran program. Several examples of slope stability analysis, which are taken from Griffiths and Lane (1999), are analyzed. The results calculated from the meshfree program are compared to the results from traditional limit equilibrium methods as given in Griffiths and Lane (1999) and finite element analyses using Abacus.

*Soil Model*

The soil parameters considered in the slope stability analysis examples include Young's modulus (E), Poisson's ratio, unit weight ($\gamma$), friction angle ($\phi'$), cohesion ($c'$) and dilation angle which values are the same as those from Griffiths and Lane (1999). In both Abacus and our meshfree program, a linear Drucker Prager model is used. The failure criterion (F) is given by:

$$F = q - p \tan\beta - d = 0 \tag{25}$$

where $p = -\dfrac{1}{3} trace(\sigma)$, $q = \sqrt{\dfrac{3}{2}(S:S)}$, $\sigma$ and $S$ are Cauchy stress and deviatoric stress tensors respectively. Parameters $\beta$ and $d$ can be converted from cohesion and friction angle from the Mohr-Coulomb model using the following equations:

$$\tan\beta = \sqrt{3}\sin\phi' \tag{26}$$

$$d = \sqrt{3}(c')\cos\phi' \tag{27}$$

In our analyses, dilation angle is set to be zero, hence a non-associated flow is assumed. Moreover, perfect plasticity is used.

*Determination of Factor-of-Safety and Slope Failure*

In traditional limit equilibrium methods, the stability of slope is reflected by means of factor-of-safety (FOS). FOS is defined as the ratio of the available strength to that required to keep the slope stable. In both finite element analyses by Abacus and our meshfree program, FOS is estimated using the strength reduction technique (Matsui and San, 1992). Original strength parameters ($\phi'$ and $c'$) would be reduced (by a sequence of factor, denoted as "*SRF*") according to equations (28) and(29). In our FE analyses by Abacus, FOS is chosen to be corresponding to the largest SRF for which a converged solution can still be obtained. Convergence of solution would be achieved when the difference in solutions from successive iterations is smaller than some pre-defined limit and also the total number of iterations must be smaller than the pre-defined maximum number of iterations. For our meshfree program, since the solution algorithm is written under a dynamic framework, convergence of solution is achieved when total kinetic energy approaches zero.

$$c'_{reduced} = c'_{original} / SRF \tag{28}$$

$$\phi'_{reduced} = \tan^{-1}(\tan\phi'_{original} / SRF) \tag{29}$$

Example 1: Homogeneous slope with no foundation layer   The soil material has a $\phi'$ of 20°, $c'$ of 10000 N/m$^2$ and $\gamma$ of 20000N/m$^3$. The height of the slope is 10m and the slope angle is 26.57°. Fig. 4 A plot of dimensionless displacement with strength reduction factor for Case 1 (Homogeneous slope)shows a plot of dimensionless displacement (EU$_{max}$/$\gamma$H$^2$) with strength reduction factor (SRF). As SRF increases, the (dimensionless) displacement increases. When the slope starts to fail, the displacement would increase excessively. For both FEM and meshfree methods, this occurs at SRF of 1.35 and 1.4 respectively. The FOS as determined using Bishop and Morgenstern (1960) by Griffiths and Lane (1999) is 1.380. It should be noted that the difference in displacements from FEM and meshfree method is due to the fact that meshfree method utilizes the dynamic framework. Fig. 5 Displacement contour plot for Case 1 (Homogenous slope) shows

the displacement contour plot from meshfree method. The critical slip surface occurs at location where contour changes rapidly.
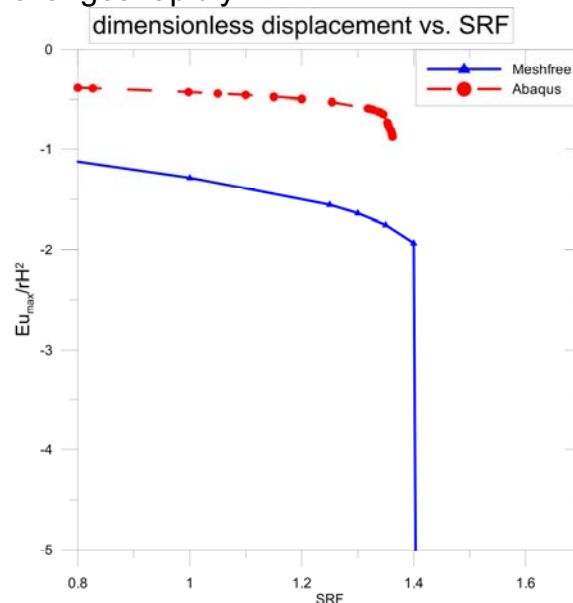


Fig. 4 A plot of dimensionless displacement with strength reduction factor for Case 1 (Homogeneous slope)
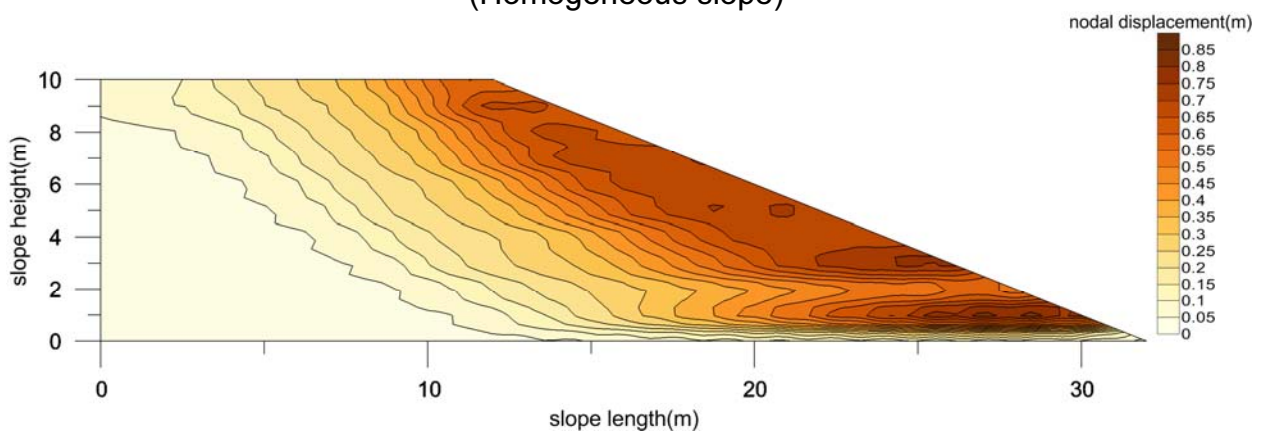


Fig. 5 Displacement contour plot for Case 1 (Homogenous slope)

Example 2: Homogeneous slope with foundation layer    The only difference between Examples 1 and 2 is that there is a 5m foundation layer. The properties of the foundation material is the same as those for the slope material. The slope is 10m high and inclines at 26.57°. According to Fig. 6 A plot of dimensionless displacement with strength reduction factor for Case 2 (Homogeneous slope with foundation layer) the FOS's as determined from Abacus and meshfree method are 1.38 and 1.4 respectively, which are essentially the same as the results from example 1. The displacement contour plot from Fig. 7 Displacement contour plot for Case 2 (Homogenous slope with foundation layer)suggests that the critical slip surface passes through the toe of the slope although there may be some local failure near the top of the slope.
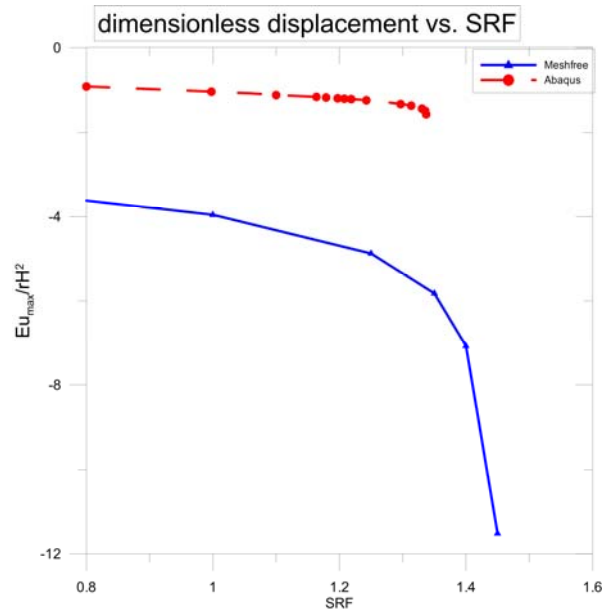
Fig. 6 A plot of dimensionless displacement with strength reduction factor for Case 2 (Homogeneous slope with foundation layer)
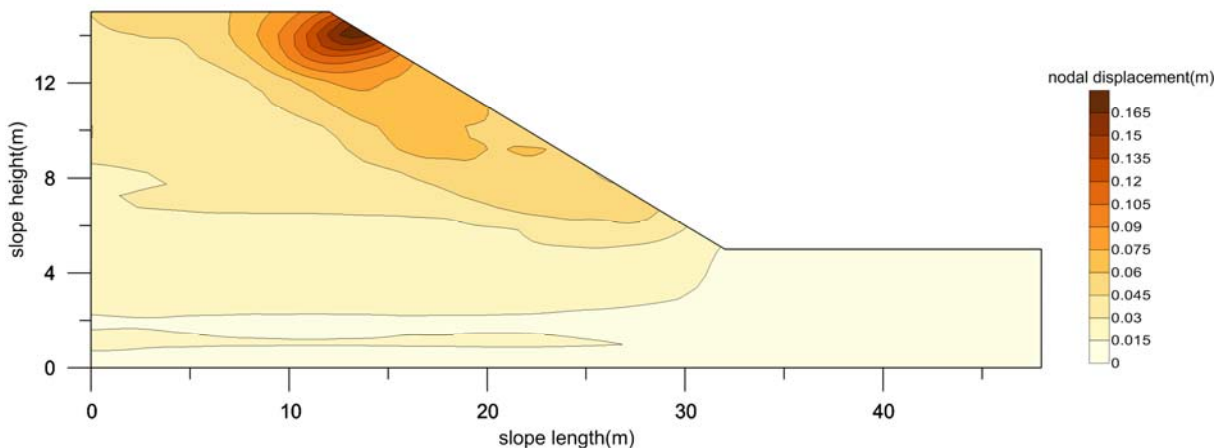


Fig. 7 Displacement contour plot for Case 2 (Homogenous slope with foundation layer)

Example 3: An undrained clay slope with a weak foundation layer   The slope is made of undrained clay material. The height and inclination of the slope are 10m and 26.57° respectively. The strength of the slope material is represented by undrained cohesion $c_{u1}$ (where $c_{u1}/\gamma H=0.25$). The thickness of the foundation layer is 10m. The shear strength of the foundation material is represented by undrained cohesion $c_{u2}$. Three values of $c_{u2}$ (at $0.6c_{u1}$, $1.5c_{u1}$, $2.0c_{u1}$ respectively) are considered. Fig. 8 A plot of dimensionless displacement with strength reduction factor for Case 3 (Undrained clay slope with foundation layer, $C_{u2}/C_{u1}=0.6$), Fig. 10 A plot of dimensionless displacement with strength reduction factor for Case 3 (Undrained clay slope with foundation layer, $C_{u2}/C_{u1}=1.5$) and Fig. 12 A plot of dimensionless displacement with strength reduction factor for Case 3 (Undrained clay slope with foundation layer, $C_{u2}/C_{u1}=2.0$)show that the FOS's as determined from FEM and meshfree method are very similar. For the case of $C_{u2}/C_{u1}=2.0$, it has been found that if we refine the number of nodes in the

meshfree model, the FOS will get closer and closer to that from FEM. The critical slip surfaces as suggested by the displacement contour plots (Fig. 9 Displacement contour plot for Case 3 (Undrained clay slope with foundation layer, $C_{u2}/C_{u1}$=0.6) Fig. 11 Displacement contour plot for Case 3 (Undrained clay slope with foundation layer, $C_{u2}/C_{u1}$=1.5) and Fig. 13 Displacement contour plot for Case 3 (Undrained clay slope with foundation layer, $C_{u2}/C_{u1}$=2.0)) are also reasonable and consistent with the results from FEM.
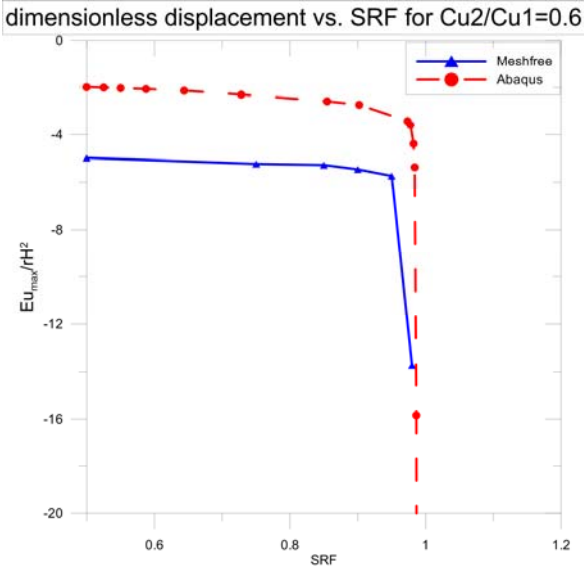


Fig. 8 A plot of dimensionless displacement with strength reduction factor for Case 3 (Undrained clay slope with foundation layer, $C_{u2}/C_{u1}$=0.6)
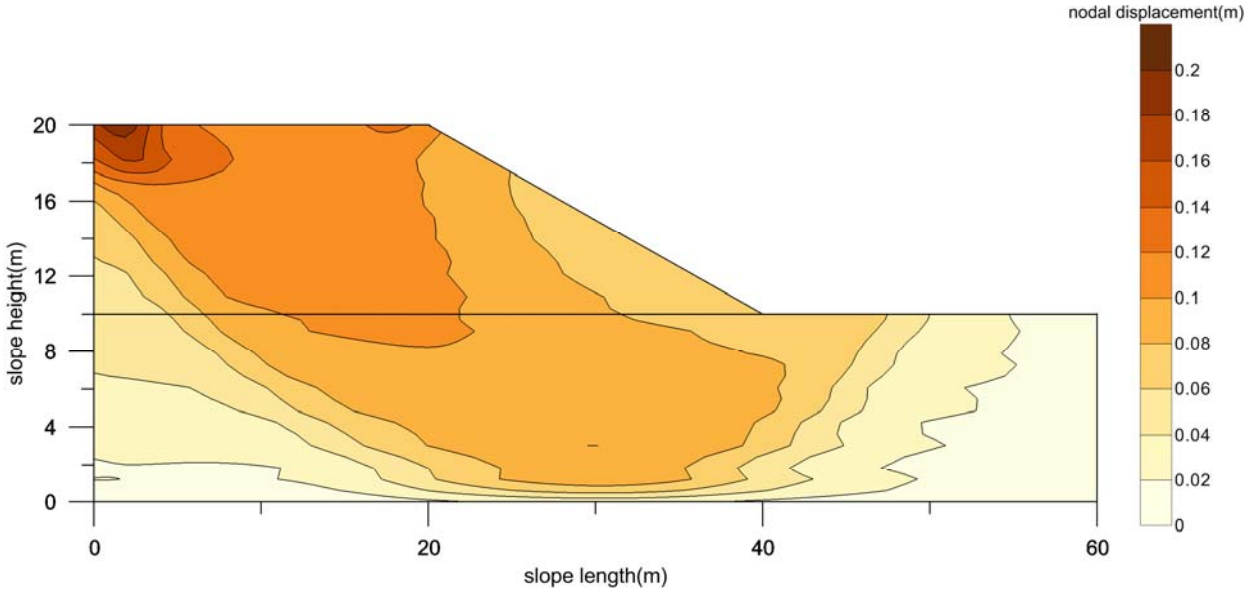


Fig. 9 Displacement contour plot for Case 3 (Undrained clay slope with foundation layer, $C_{u2}/C_{u1}$=0.6)
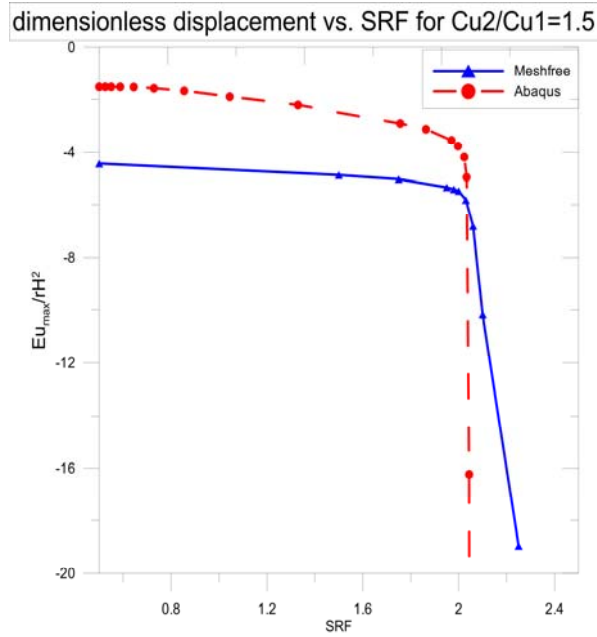
Fig. 10 A plot of dimensionless displacement with strength reduction factor for Case 3 (Undrained clay slope with foundation layer, $C_{u2}/C_{u1}$=1.5)
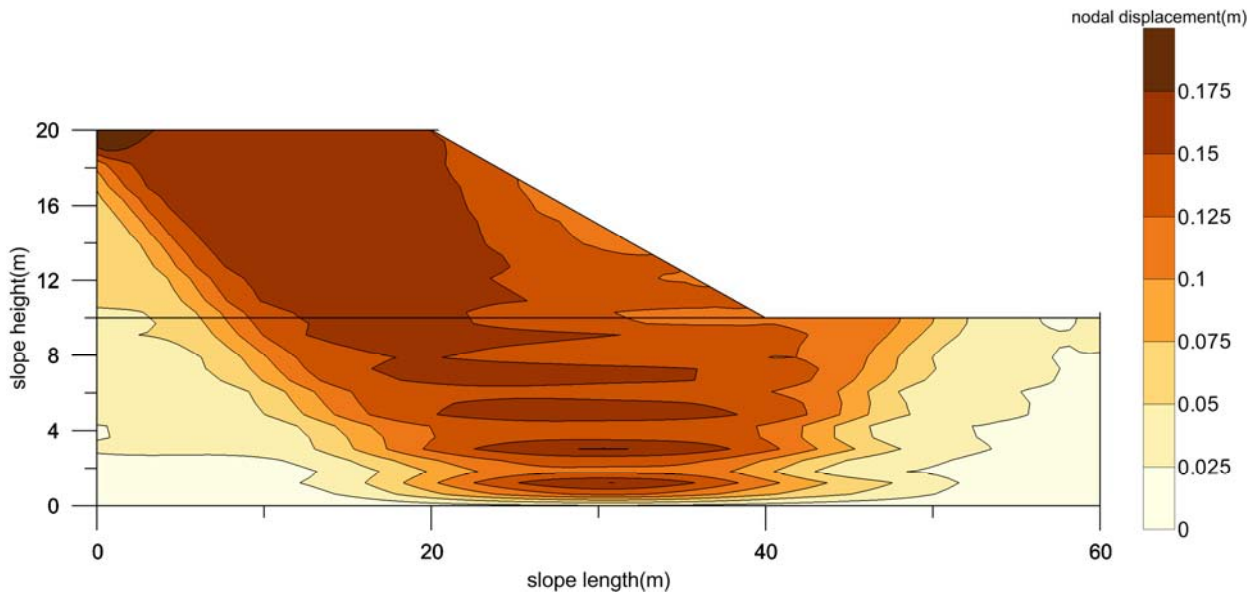


Fig. 11 Displacement contour plot for Case 3 (Undrained clay slope with foundation layer, $C_{u2}/C_{u1}$=1.5)
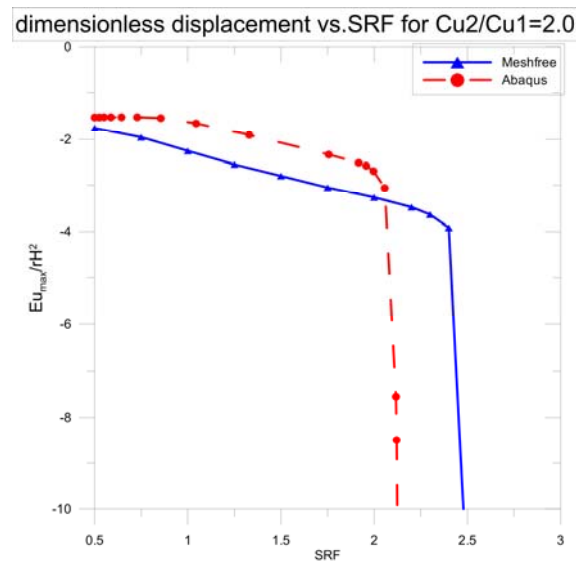
Fig. 12 A plot of dimensionless displacement with strength reduction factor for Case 3 (Undrained clay slope with foundation layer, $C_{u2}/C_{u1}=2.0$)
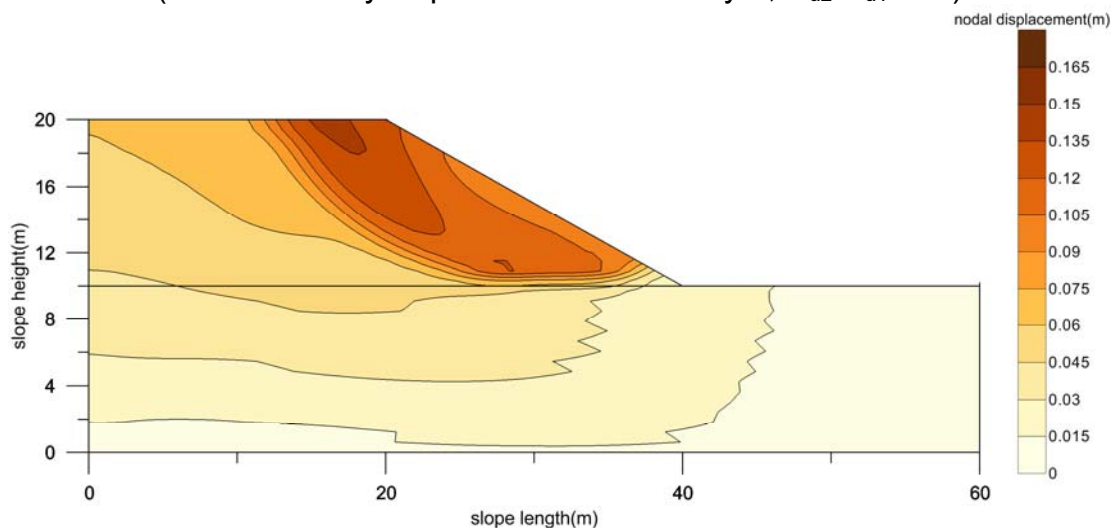


Fig. 13 Displacement contour plot for Case 3 (Undrained clay slope with foundation layer, $C_{u2}/C_{u1}=2.0$)

## POST-FAILURE ANALYSES

Due to the problem imposed by mesh distortion, FEM analyses are only capable of modeling condition up to failure or finite deformation. Here, we are going to demonstrate that meshfree method is capable of modeling post-failure behavior when deformation is large.

In this example, the slope inclines at 63.4°. To show that the meshfree method can still work even after the soil material has failure, uniform pressure is gradually increased and applied on the top of the slope until the slope fails. As observed from Fig. 14, soil materials from the failed slope slide down the slope and accumulate at the bottom of the slope.
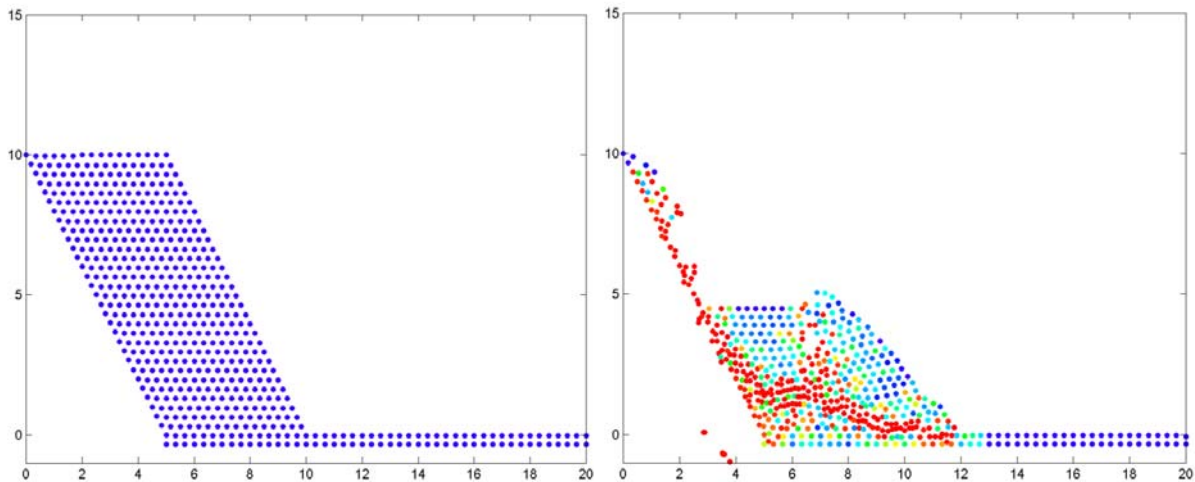
Fig. 14. post-failed slope modelled by meshfree method

## CONCLUSION

Slope stability analyses have been performed using meshfree method. Factor-of-safety estimates are found to be consistent between FEM and meshfree method. Similar to FEM, meshfree method retains the benefits over traditional LEM, i.e., no assumption about critical slip surface needs to be made prior to analysis and failure occurs naturally at zones where applied shear stress exceed shear strength. Moreover, the last example presented in this paper demonstrated that meshfree method can be used to model the condition after slope failure (or large deformation) has occurred.

## REFERENCES

Bishop, A.W. and Morgenstern, N.R.  (1960). "Stability coefficients for earth slopes," *Geotechnique*, 5 (1), 7-17

Chen, J. S., Pan, C., Wu, C. T., Liu, W. K.. (1996) "Reproducing Kernel Particle Methods for large deformation analysis of non-linear structures." *Comput. Methods Appl. Mech. Engr*g. 139 195-227

Griffiths, D.V. and Lane, P. A. (1999). "Slope stability analysis by finite elements," *Geotechnique*, 49(3), 387-403.

Guan, P., Chen, J. S., Wu, Y., Teng, H., Gaidos, J. Hofstetter, K. Alsaleh, M. (2009) "A Semi-Lagrangian Reproducing Kernel Formulation for Modeling Earth Moving Operations," *Mechanics of Materials*, Vol. 41, pp. 670-683

Guan, P.C., Chi, S.W., Chen, J.S., et al. (2011). "Semi-Lagrangian reproducing kernel particle method for fragment-impact problems," *International Journal of Impact Engineering*, *Vol*. **38**(12), 1033-1047.

Liu, W. K., Jun, S., Zhang, Y. F., (1995). "Reproducing kernel particle methods." *International Journal of Numerical Methods in Fluids*, 20:1081-1106

Matsui, T. and San, K.C. (1992). "Finite element slope stability analysis by shear strength reduction technique," *Soils and Foundations*, 32(1), 59-70.